Component shape optimisation for enhanced non-destructive testing

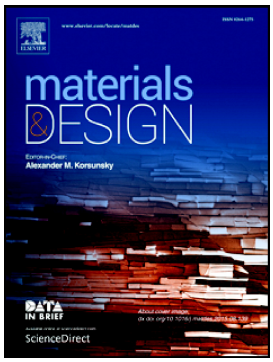

Component shape optimisation for enhanced non-destructive testing

J. Singh, A.J. Mulholland, K.M.M. Tant, T. Stratoudaki, A. Curtis, W. Ijomah, J.F.C. Windmill

PII: S0264-1275(20)30576-1

DOI: https://doi.org/10.1016/j.matdes.2020.109041

Reference: JMADE 109041

To appear in: *Materials & Design*

Received date: 1 June 2020

Revised date: 13 July 2020

Accepted date: 4 August 2020

Please cite this article as: J. Singh, A.J. Mulholland, K.M.M. Tant, et al., Component shape optimisation for enhanced non-destructive testing, *Materials & Design* (2020), https://doi.org/10.1016/j.matdes.2020.109041

Component Shape Optimisation for Enhanced Non-Destructive Testing

J. Singh[1,*], A. J. Mulholland[2], K. M. M. Tant[1], T. Stratoudaki[1], A. Curtis[3], W. Ijomah[1], J. F. C. Windmill[1]

[1] University of Strathclyde, Glasgow, UK

[2] Department of Engineering Mathematics, University of Bristol, UK

[3] School of Geosciences, University of Edinburgh, UK

[*] Corresponding author: jonathan.singh@strath.ac.uk

July 13, 2020

Abstract

Determining an optimal component design is fundamental to many applications including many of those in the aerospace, automotive and civil engineering industries. Previously, the compatibility of the component with future non-destructive testing (NDT) requirements has not been considered at the design stage. As a result, NDT operators are often challenged to reliably inspect components with complex geometries. In this paper, a framework is proposed for the optimisation of a component's shape to maximise the sensitivity and coverage of an interrogating ultrasonic wave, thus enhancing the ability to non-destructively image defects. The design of beam cross-sections are optimised using both a low-dimensional parameterisation with a genetic algorithm, and the level set method which enables more degrees of freedom in the component shape parameterisation. Images of flaws computed using the total focusing method show an 8 dB improvement in the signal to noise ratio for the optimised component as well as a five-fold improvement in the estimate of flaw size. These results show that the NDT-optimised design of components can provide significant improvements in flaw imaging. This in turn assists in extending the lifespan of in-service components and indeed their remanufacturability, which is both environmentally and economically advantageous.

Key words: *Design, Shape optimisation, Level set method, Non-destructive testing, Ultrasound*

1 Introduction

The development of sustainable methods for the manufacture of components is critical across all engineering disciplines. One environmentally friendly and economically viable approach is *remanufacturing*; the process of bringing a used product to a state that performs at least at the same level as the original product, and is therefore issued an as-new warranty [19, 27].

The remanufacturing procedure is as follows: a product is stripped down to its individual components; the components are cleaned, assessed, remanufactured and restored; then the product is rebuilt and performance tested [19]. Lund [27] indicates that 85 % of the mass of a remanufactured product may be sourced from used components, and requires 50–80 % less energy to produce, providing a 20–80 % production cost saving in comparison to conventional manufacturing. The principle of design-for-remanufacturing (DfREM) recognises the importance of the initial component design in aiding the steps involved in the remanufacturing process [15].

During the remanufacturing assessment stage, the detection of any internal defects is critical; both production costs and environmental impact are reduced when the level and reliability of inspection is enhanced, so that defective components are also not propagated through the manufacturing process. Non-destructive evaluation or testing (henceforth, NDT) is a term that describes a range of methods that evaluate components non-invasively [38]. The dominant modality is ultrasonic NDT, which uses high-frequency mechanical waves to image the interior of a component [41]. These methods allow for inexpensive, near real-time, and high resolution images of a component's interior to be generated and any internal defects detected [6, 26], even in heterogeneous material [46, 47, 48]. However, although reliable NDT is key for maintenance and life extension of a component, the suitability of a component for NDT is not currently considered in the optimisation of most component's design [47].

In the last decade, ultrasonic NDT has seen a rapid increase in the use of ultrasonic phased arrays for standardised inspection of components [20, 53]. The advantage of using arrays is increased imaging quality as the array can control the directivity and focus of the ultrasound by varying the time delay between firings of the array elements. However, in general, ultrasonic phased arrays are based on piezoelectric transduction, which has certain limitations. For example, the transducers often require the use of a coupling medium between the tested component and the testing equipment and are constructed from a fixed number of elements, with a predefined (normally planar) shape. These constraints mean that the transducer based phased arrays cannot be used on components with complex geometries or in settings where access to the surface of the

component is restricted.

Laser ultrasound offers an alternative, non-contact method, for the transmission and reception of ultrasonic waves [12, 45, 51]. The light from a pulsed laser induces a mechanical wave in the component through localised heating and thermal expansion at the component surface [40]. The transmitted waves are then detected using laser interferometry, which uses the phase shift of laser light to detect very small displacements at the component surface, offering a completely non-contact ultrasonic inspection system [31]. There are several advantages to using this method. First, as there is no mechanical contact, laser ultrasound is not affected by any impedance mismatch between the component and transducer. Second, laser ultrasound can be used for components with more complex geometries and in testing areas where surface access is restricted, where piezoelectric transducers, with fixed sizes and shapes, constrain the range of testable component shapes [49, 54].

Laser phased arrays can be synthesised in post processing: by controlled movement of a generating and receiving pair, an array of sensors can be synthesised [5, 44]. This realises a comparable amount of array data to that generated using conventional, transducer based phased arrays. In particular, Stratoudaki et al. [44] captured the full matrix of source-receiver time domain signals (i.e. all $N \times N$ ultrasonic generation and detection signal pairs for source/receiver positions), and applied the total focusing method (TFM) imaging algorithm, demonstrating increased ultrasonic imaging quality compared to other laser ultrasonic techniques. Thus, laser ultrasonic phased arrays offer the advantages of remote ultrasonic testing with the added flexibility of choosing the number of elements and their distribution on any complex shape geometry [8, 36] and without compromising image quality. It seems appropriate therefore to use laser induced ultrasound in the design-for-testing framework proposed in this paper.

Recently, additive manufacturing (AM) has enabled new families of intricate structures to be manufactured [14]. The resulting complexity of the component, however, exposes the limitations of conventional piezoelectric NDT methods. On the other hand, the ability of laser ultrasound to test such complex structures enables AM to facilitate NDT: as the manufacturing of more complex component shapes that improve suitability for NDT is no longer a barrier, intricate structures can be manufactured in a cost effective way and with less material waste. There are also several considerations in the design of a component to best aid the AM process (design-for-AM - DfAM) [37].

This paper proposes and demonstrates a design-for-testing (DfT) framework for the optimisation of a component's shape with respect to NDT suitability, which is complementary to and may be used in parallel with DfREM and DfAM frameworks. DfT frameworks are commonly implemented in electrical engineering for the design of circuit boards [23] and software engineering for the design of testable programs [39]. However, this is the first implementation of an automated DfT framework for ultrasonic testing. Two algorithms for shape optimisation are implemented within our framework: a genetic algorithm approach for a design parameterisation with a low number of degrees of freedom [52], and a deterministic optimisation approach, coupled with a more complex design parameterisation defined using a level set method [1, 28, 35, 42]. This method is widely used in a range of application areas including aerospace and structural engineering [13, 21], and allows smooth perturbations to the boundary of a shape. In this study, the admissible shapes are constrained using a design envelope and the evolution of optimal shapes when the design envelope width is increased (allowing larger deviations from the initial component shape) is investigated.

The paper first describes the optimisation problem, and the analytical approach for generating ultrasonic sensitivity maps for laser induced ultrasound. A suitable objective function is defined and an optimisation method chosen, and the method is tested across a range of two-dimensional cross-sections through various beams which are commonly found in civil engineering applications [4, 22]. The total focusing method [16] is then employed, to quantify the improvement in the imaging of a point scatterer embedded in the internal structure of an optimised component. This framework lends itself to being coupled to other design or testing constraints or demands and this paper also discusses the optimal positioning of the laser source/receiver locations at the component's surface.

2 Method

Consider a component with spatial domain Ω, which is to be evaluated using ultrasonic non-destructive testing (NDT). A mechanical force is laser induced at a point s on the component boundary $\partial\Omega$ and the mechanical vibration is recorded (via laser interferometry) as a function of time t at point $r \in \partial\Omega$ (Figure 1a). Define $\mathbf{\Gamma}$ as the vector of all s and r positions (which in this work are co-located), so that $s, r \in \mathbf{\Gamma}$. Typically, all points s and r act in turn as both sources and receivers, in a process known as *full matrix capture* (FMC, see Holmes et al. [17, 18]). Now consider the ultrasonic sensitivity E of a component, which is a measure of the

effectiveness of ultrasound to resolve a defect at any position $\mathbf{x}$ within the component. The sensitivity E is a function of the distribution of source and receivers Γ, the material properties Ξ, and the shape of the component domain Ω, so $E(\mathbf{x},\Gamma,\Xi,\Omega)$. To simplify matters here, for the following shape optimisation experiments, the material properties Ξ are constant and the sensor coverage Γ is fixed to the entire boundary of the component $\partial\Omega$ with maximum coverage (at every pixel on the boundary).

The objective is to perturb the boundary of the component $\partial\Omega$ in order to improve defect detection and characterisation capabilities using ultrasonic NDT. Specifically, this involves determining the minimum sensitivity (E^* say) observed over all $\mathbf{x} \in \Omega$ and finding the design Ω^* that maximises E^*, thus removing ultrasonic blind spots within the component. That is

$$E^* = \min_{\mathbf{x}\in\Omega} : E(\mathbf{x},\Gamma,\Xi,\Omega) \tag{1}$$

and

$$\Omega^* = argmax_{\Omega\in K} : E^*(\Gamma,\Xi,\Omega) \tag{2}$$

[[Image]]

Figure 1: a) Schematic diagram of a component domain Ω with the boundary $\partial\Omega$, where the ultrasonic energy is generated at the source s and detected at the receiver r, and Γ is the set of source and receiver locations for a given experiment. b) Illustration of the design envelope with width δ around the initial boundary of a component.

subject to the volume constraint $V(\Omega) = V_{req}$, and where K is the set of all admissible shapes. To preserve the primary function of a component, it is desirable to constrain the optimisation in Equation (2) so that the perturbations to the boundary $\partial\Omega$ of the component are performed within the design envelope K (Fig. 1b).

The shape optimisation of an I-beam is discussed in Section 2.2, where there are just a few degrees of freedom in the parameters describing the component's shape. A more general method, where the component shape is parameterised with a level set function, is then presented in Section 2.3.

2.1 Analytical method for laser induced ultrasound sensitivity

[[Image]]

Figure 2: Example directivity patterns for laser induced ultrasound in steel for: a) the generation of longitudinal waves (Equation (3)) and b) transverse waves (Equation (4)); the out of plane

reception of c) longitudinal waves (Equation (5)) and d) transverse waves (Equation (6)).

[[Image]]

Figure 3: a) Schematic illustrating the method for computing the sensitivity map E for a given component spatial domain Ω, by computing the recorded amplitude of a point scatterer at $\mathbf{x}$, with source location s and receiver location r and using the distance d_s / d_r and angle θ_s / θ_r to the scatterer. b) Example sensitivity map E_{LL} for the shape Ω, using Equation (9). The directivity amplitude values are normalised to the scattering amplitude.

To perform an optimisation of a component with domain Ω, the sensitivity of ultrasound waves as a function of $\mathbf{x}$ must be computed. Here, the sensitivity map of a component is generated using analytical expressions for the transmission and reception sensitivity of laser induced ultrasound. Using laser induced ultrasound allows energy to be generated and detected at any point on the surface of a component for which we have line of sight. Point sources have been used for a range of practical applications [40], however in some cases it is desirable to use a line source which can reduce the peak optical intensity keeping it below the destructive ablation threshold of the material, and facilitate wave directivity [44].

To illustrate the approach, this paper restricts attention to the two-dimensional cross-section of a component. Expressions for the excitation of longitudinal L and transverse T wave displacements in a two-dimensional medium using a thermoelastic source [11], as a function of angle θ (measured normal to the cross-section boundary) are given by [3, 34]

$$S_L(\theta) = \frac{\sin\theta \sin 2\theta (\kappa^2 - \sin^2\theta)^{1/2}}{2\sin\theta \sin 2\theta (\kappa^2 - \sin^2\theta)^{1/2} + (\kappa^2 - 2\sin^2\theta)^2} \tag{3}$$

$$S_T(\theta) = \frac{\sin 2\theta \cos 2\theta}{\cos^2 2\theta + 2\sin\theta \sin 2\theta (\kappa^{-2} - \sin^2\theta)^{1/2}} \tag{4}$$

where $\kappa = V_L / V_T$, the ratio of longitudinal (V_L) to transverse wave velocity (V_T) in the host material. A laser vibrometer, sensitive to the out-of-plane component of displacement (that is, in two dimensions normal to the component boundary) can be used for detecting the arriving waves. The sensitivity of detecting longitudinal and transverse waves is given by [29]

$$R_L(\theta) = \frac{\cos\theta (\kappa^2 - 2\sin^2\theta)}{F_0(\sin\theta)} \tag{5}$$

$$R_T(\theta) = \frac{\sin 2\theta(\kappa^2 \sin^2\theta - 1)^{1/2}}{F_0(\kappa \sin\theta)} \tag{6}$$

where F_0 is defined as $F_0(\xi) = (2\xi^2 - \kappa^2)^2 - 4\xi^2(\xi^2 - 1)^{1/2}(\xi^2 - \kappa^2)^{1/2}$.

An example of the transmission and reception sensitivity patterns for longitudinal and transverse waves is shown in Figure 2 using the material properties of steel ($V_L = 5900$ m/s and $V_T = 3250$ m/s). In this case, the maximum transmission amplitude is at $\theta_s = \pm 60^\circ$ for longitudinal waves and $\theta_s = \pm 32^\circ$ for shear waves, and the maximum sensitivity for received longitudinal waves is at $\theta_r = 0^\circ$ and $\theta_r = \pm 32^\circ$ for transverse waves. For simplicity, this paper only considers the longitudinal wave components in the calculation of wave sensitivity (denoted E_{LL}).

There are many methods for taking the time domain full matrix capture measured data and creating an image of the component which is being tested via post-processing. The most commonly used of these is the total focusing method (TFM), see Holmes et al. [16]. In this method, the signals from all source-receiver pairs in the array are summed to synthesise a focus at every point within Ω in a discretised grid, assuming a constant (homogeneous) and isotropic medium. Take $u_{sr}(t)$ to be the signal recorded at receiver r as transmitted at source s. For n^2 source-receiver pairs, the intensity of the TFM image I is given by [16]

$$I(\mathbf{x}) = \left| \sum_{s=1}^{n} \sum_{r=1}^{n} \mathcal{H}(u_{sr}(t_{sr}(\mathbf{x}))) \right|, \mathbf{x} \in \Omega \tag{7}$$

where $\mathcal{H}(\cdot)$ denotes the Hilbert transform. The double summation is over all combinations of source-receiver pairs and the delay term is given by

$$t_{sr}(\mathbf{x}) = \frac{d_s(\mathbf{x}) + d_r(\mathbf{x})}{V_L} \tag{8}$$

where $d_s(\mathbf{x})$ and $d_r(\mathbf{x})$ are the distances from the source and receiver to the point $\mathbf{x}$, respectively.

Using equations (3-6), a sensitivity map $E_{LL}(\mathbf{x})$ [44] for longitudinal wave displacements in two dimensions is given by

$$E_{LL}(\mathbf{x}, \Omega) = \frac{1}{n^2} \left| \sum_{s=1}^{n} \sum_{r=1}^{n} \frac{S_L(\theta_s(\mathbf{x})) R_L(\theta_r(\mathbf{x}))}{[d_s(\mathbf{x}) d_r(\mathbf{x})]^{1/2}} \right| \tag{9}$$

where the denominator of the summand represents the two-dimensional geometric spreading of wave energy. This expression describes the expected amplitude of a perfect point defect (or point scatterer, where the scattering amplitude is fixed and constant in every direction) at position $\mathbf{x}$. An example sensitivity map is shown for a steel square in Figure 3b, where sources and receivers are placed around the full boundary. $E_{LL}(\mathbf{x})$ can be used in Equation (1), allowing the calculation of a misfit function for the subsequent optimisation. In the case of components with a concave shape (i.e., where any interior vertex angles are greater than 180°), some paths from source s or receiver r locations to point $\mathbf{x}$ intersect the component boundary $\partial\Omega$. For the algorithm implemented here, the summand in the numerator in Equation (9) is set to zero and is therefore not included in the double summation.

There are a few limitations to this method. For example, only first-order scattering is considered, no reflections from the boundary of the component are accounted for, and only a single homogeneous and isotropic material is considered. This approach also does not account for attenuation of energy during propagation. However, each of these drawbacks can be accounted for in the design process if more accurate prior information about the component's properties is available, and, at the expense of additional computation, the model can be augmented accordingly. The simplicity of our model allows for rapid computation of sensitivity maps, and this allows for a range of computationally efficient optimisation methods to be used and compared in the absence of detailed prior information about each component.

2.2 Shape optimisation algorithm: Parametric optimisation

A common method in design engineering for finding an optimal shape for a component is to take a low degree of freedom parameterisation of a shape (e.g., for the design of airfoils, see Song and Keane [43]), and optimise its properties using, for example, genetic algorithms, differential evolution or CMA-ES methods [25, 32]. This approach is taken here for a two-dimensional cross-section through an I-beam (also known as H-beam or universal beam). This is a widely used component in the construction industry, which is therefore widely tested using ultrasonic NDT. The parameterisation shown in Figure 4 is used, where the component spatial domain Ω is a function of 5 parameters: the length L, width W, flange thickness F, web thickness T and the corner depth C, that is $\Omega = f(\mathbf{y})$ where $\mathbf{y} = (L, W, F, T, C)$. Equally spaced sources and receivers are positioned around the boundary at a spacing of 1 pixel and the material properties Ξ

of steel (V_L = 5900 m/s and V_T = 3250 m/s) are assigned throughout the domain.

The calculation of the sensitivity map E_{LL} (Equation (9)) contains the distances from a point $\mathbf{x}$ to the sources and receivers. As these distances decrease, the sensitivity increases. Therefore, if a component size was to decrease, the distance from any central point to the boundary decreases and sensitivity increases. Thus, a constraint on the required volume (V_{req}) must be included in the optimisation to ensure that the component does not simply shrink to a point mass to maximise sensitivity.

[[Image]]

Figure 4: Illustration of the parameterisation for the cross-section of an I-beam, with five free parameters: length (*L*), width (*W*), flange thickness (*F*), web thickness (*T*) and corner depth (*C*); Ω and $\partial\Omega$ are as in Figure 1.

Table 1: Output parameters from the parametric optimisation (Equation (11)), for varying envelope widths δ when finding the optimal length (*L*), width (*W*), flange thickness (*F*), web thickness (*T*) and corner depth (*C*). Units are pixels in the images in Figure 5.

	Initial	δ = 2	δ = 10	δ = 20	δ = 28
L	80	80	83	82	69
W	50	50	45	47	45
F	9	9	9	4	5
T	18	18	17	22	25
C	1	2	2	5	4
E^*_{LL}	3.08	3.73	3.76	5.01	5.21

[[Image]]

Figure 5: Resulting shapes following the minimisation of the objective function (Equation (11)) via a genetic algorithm with increasing envelope bounds: a) Initial shape (the domain is composed of 100×100 pixels), b) envelope width δ =2, c) δ =10, d) δ = 20, and e) δ =30. f-j) the corresponding sensitivity maps (E_{LL}) and k) the minimum sensitivity E^*_{LL} as a function of envelope width δ. All final, optimised cross-section volumes are equal to that of the initial shape.

The minimum sensitivity of longitudinal waves over the domain E_{LL}^{*} is defined as

$$E_{LL}^{*}(\Omega(\mathbf{y})) = \min_{\mathbf{x}\in\Omega} : E_{LL}(\mathbf{x}, \Omega(\mathbf{y})). \tag{10}$$

The material properties Ξ are constant, and the source/receiver locations Γ are fixed to the entire boundary $\partial\Omega$, so that a source/receiver is located at every boundary pixel. Γ is therefore a function of Ω), so we omit the dependence on Γ and Ξ here. The optimal set of parameters $\mathbf{y}^{*}$, and therefore the optimal shape $\Omega^{*}(\mathbf{y}^{*})$, are given by

$$\mathbf{y}^{*} = \operatorname{argmin}_{\mathbf{y}\in K} : \Phi(\Omega(\mathbf{y})) \tag{11}$$

where the misfit function $\Phi(\Omega(\mathbf{y})) = \lambda \left| V_{req}(\Omega) - V(\mathbf{y}) \right| - E_{LL}^{*}(\Omega(\mathbf{y}))$ is a combination of the volume constraint and the minimum sensitivity, and where λ is a weighting factor on the volume constraint, $V(\Omega)$ is the solid material volume for the domain Ω, V_{req} is the required volume and K is the set of admissible shapes.

A genetic algorithm [52] is employed to find the set of parameters that solve Equation (11), and information on the genetic algorithm is provided in the appendix. The implementation allows upper and lower bounds for each parameter to be applied, which enables the envelope bounds around an initial shape to be imposed (as in Fig. 1b). The initial I-beam shape (Fig. 5a), is given by the initial parameter values detailed in Table 1. The genetic algorithm optimisation is performed with four increasing envelope widths δ (2, 10, 20 and 28 pixels) and using $\lambda = 0.5$. The optimal shapes using each envelope bound are shown in Figures 5b-e and the parameters are detailed in Table 1; the domains shown are 100×100 pixels. In all cases, the resulting minimum sensitivity E^{*} for the optimal I-beam parameterisation is an improvement from the initial shape and the volume constrained is satisfied ($V_{req}(\Omega) - V(\mathbf{y}) = 0$). As the envelope width δ increases, a broader range of parameters are admissible and the minimum sensitivity E^{*} further increases (shown in Figure 5k) until width $\delta = 28$ where we obtain a 70% increase in minimum sensitivity E_{LL}^{*} compared to the original design. The regions of lowest ultrasonic sensitivity are concentrated around concave corners (where the interior angles are greater than 180°, visible in the sensitivity maps E_{LL} shown in Fig. 5f-j). The designs with a higher minimum sensitivity E_{LL}^{*} exhibit smaller interior angles at the concave corners ($\delta = 20$ (Figs 5d and i) and $\delta = 28$ (Figs 5e and j)). This approach is intuitive and effectively demonstrates the framework for optimising the shape

of a component for the ease of NDT. However, such low degrees of freedom parameterisations only allow a limited range of possible perturbations to a component's shape and so below a different approach is explored.

2.3 Shape optimisation algorithm: Level set method

An alternative method for optimising a component's shape is to parameterise the shape using a continuum approach. One such approach is the Level Set Method [1, 42, 50]. The method expresses a curve (2D) or surface (3D), as a zero level set of a higher-dimensional function (level set function ψ) in an implicit manner (the function ψ is precisely one dimension higher than the domain being optimised). The level set function has the following properties

$$\psi(\mathbf{x}) \begin{cases} < 0 & \text{if } \mathbf{x} \in \Omega \\ = 0 & \text{if } \mathbf{x} \in \partial\Omega \\ > 0 & \text{if } \mathbf{x} \notin \Omega \end{cases} \tag{12}$$

where $\mathbf{x}$ is any point in the design domain, and $\partial\Omega$ is the boundary of Ω.

Any change to the boundary shape during the optimisation is performed via the evolution of the level set function ψ [42]. Figure 6 illustrates the relationship between the level set function ψ and a one-dimensional domain Ω, and shows how perturbations to ψ affect the length of Ω. The temporal and spatial evolution of ψ in the optimisation is governed by

$$\frac{\partial \psi}{\partial t} = -v\,|\nabla \psi| \tag{13}$$

where v is a scalar field over the design domain which determines the geometric motion in the normal direction of the boundary of the structure and t denotes the time evolution of ψ. The level set function ψ is first initialised as a signed distance function from the boundary of the initial shape $\partial\Omega_0$ (illustrated in Figure 6a). An upwind finite-difference scheme is used to solve Equation (13) numerically (see Challis [7] for algorithm details). The time step Δt for the finite difference scheme is constrained by the Courant-Friedrichs-Lewy (CFL) stability condition: $\Delta t \le h / \max|v|$, where h is the minimum spatial distance between spatial grid points [42]. The discrete level set topology optimisation algorithm for compliance minimisation of Challis [7] is adapted here to suit an ultrasound sensitivity maximisation problem, by defining v_i (where subscript i denotes the i^{th} iteration of the level set minimisation) as

[[Image]]

Figure 6: Illustration describing the relationship between the level set function ψ (blue) and the component with a one-dimensional shape Ω (red). The mathematical relationship is described by Equation (20). As the level set function is perturbed so that more points x decrease below zero, the eigen-length of Ω increases.

$$v_i(\mathbf{x}) = C_i(\mathbf{x}) - \lambda_i - \frac{1}{\Lambda_i}[V_i(\Omega_i) - V_{req}] \tag{14}$$

where $V_i(\Omega_i)$ is the solid material volume for the current domain Ω_i, and V_{req} is the required volume. The optimisation minimises $C_i(\mathbf{x})$ locally at $\mathbf{x}$ subject to the volume constraint $V_{req} = V_i(\Omega_i)$; the objective here is to *maximise* the ultrasonic sensitivity and so C is defined as $1/E_{LL}$. The values λ_i and Λ_i are augmented Lagrangian parameters used to constrain the optimisation [28]. They update after each iteration according to

$$\lambda_{i+1} = \lambda_i + \frac{1}{\Lambda_i}[V_i(\Omega_i) - V_{req}] \tag{15}$$

and

$$\Lambda_{i+1} = \alpha\Lambda_i \tag{16}$$

where $\alpha \in (0,1)$ is a fixed parameter so that at later stages in the optimisation $1/\Lambda_i$ becomes large and more emphasis is put onto the volume constraint. The parameter λ_i stores values of the previous iteration acting as a momentum term to stabilise the optimisation. A demonstration of the evolution of the terms v, the volume $V_i(\Omega)$, and ultrasonic coverage E_{LL} is provided in Section 3.1. To constrain the possible shapes to only those within a design envelope around the initial shape boundary, a binary mask $M(\mathbf{x}) \in \mathbb{Z}_2$ is used, where $M(\mathbf{x}) = 1$ only if $\mathbf{x}$ lies within the allowable envelope. The mask $M(\mathbf{x})$ is applied to Equation (13) so that the level set function at $\mathbf{x}$ only changes if $M(\mathbf{x}) = 1$. Hence

$$\frac{\partial \psi}{\partial t} = -vM\,|\nabla \psi|. \tag{17}$$

As ψ at $\mathbf{x}$ does not change outside of the design envelope ($M(\mathbf{x}) = 0$), these values of ψ do not deviate from their initial values of a signed distance function from the boundary $\partial\Omega$ (shown in Fig. 6). Therefore the component boundary $\partial\Omega$ can only exist within the envelope, where $M(\mathbf{x}) = 1$.

The criteria used for convergence of the algorithm is

$$V_i(\Omega_i) - V_{req} < \varepsilon_1 \tag{18}$$

and

$$\frac{|\int_\Omega C_i(\mathbf{x})d\mathbf{x} - \int_\Omega C_j(\mathbf{x})d\mathbf{x}|}{\int_\Omega C_i(\mathbf{x})d\mathbf{x}} < \varepsilon_2, \forall j \in \{i-5,\ldots,i-1\} \tag{19}$$

where we have chosen $\varepsilon_1 = 0.005$ and $\varepsilon_2 = 0.01$.

3 Results

3.1 Unconstrained shape optimisation

To illustrate the level set method optimisation approach, we first consider its application to a square initial shape (or cross-section of a square rod, see Fig. 7a) and perform an unconstrained optimisation where the masking term M in Equation (17) consists only of ones ($M(\mathbf{x}) = 1$ $\forall \mathbf{x} \in D$, where D is the total design domain), and therefore any component shape which lies completely within the domain is admissible. The required volume V_{req} is set to the volume of the initial shape (in the example shown $V_{req} = 0.2$); thus volume is preserved. The design domain D is discretised with 100×100 pixels and the initial augmented Lagrangian parameters are $\alpha = 0.9$, $\lambda_0 = -0.01$ and $\Lambda_0 = 1000$. The top row of images in Figure 7 shows the evolution of component spatial domains Ω at certain stages during the optimisation, where the final shape is obtained after 106 iterations and is shown in Figure 7d. The second row of images show the corresponding sensitivity maps E_{LL} and the third row gives the corresponding level set functions ψ. Figures 7m, n and o show the evolution of the minimum sensitivity within the component (E^*_{LL}), the mean of the velocity term v_i (Eqn. (14)) and the volume residual $V_i(\Omega_i) - V_{req}$ as a function of algorithm iteration i. In the first iteration ($i = 0$), the initial volume is chosen such that the volume constraint in Equation (14) is satisfied, $C(\mathbf{x})$ is positive and λ is negative. Therefore v is positive, the right hand side of Equation (13) is negative, and so the function ψ decreases and the size of the domain Ω increases (in a similar manner to that shown schematically in Figure 6) ensuring the design shifts away from the initial shape. In subsequent iterations, the volume constraint in Equation (14) increases where $V_i > V_{req}$ (Ω_i is too large) and decreases where

$V_i < V_{req}$ (Ω_i is too small), resulting in an oscillatory motion and eventual stabilisation at a (possibly local) minimum, as the volume fraction residual tends to zero. The mean of the scalar field v (which determines the rate of change of the shape as given by Equation (13)) also tends to zero (Fig. 7n), and this corresponds to the term $C(\mathbf{x})$ being minimised (and therefore $E_{LL}(\mathbf{x})$ being maximised). The minimum sensitivity E_{LL}^* increases by approximately 30% from the initial shape (Fig. 7i) and the volume constraint is satisfied (Fig. 7j). In the intermediate stages (plots (c) and (g)), shapes are found with a higher E_{LL}^* compared to the final shape, however these shapes violate the volume constraint. Intuitively, the final shape is approximately a disk of radius $\sqrt{V_{req}/\pi}$. The compute time for this optimisation algorithm on a standard desktop computer (i7-8650U processor) running in MATLAB (2019b) is approximately 30 seconds.

[[Image]]

Figure 7: a-h) Demonstration of the shape optimisation algorithm using the level set method. The first row shows component domain Ω, the second and third rows show the respective sensitivity maps E_{LL} and level set functions ψ. The initial shape is shown in panel (a) at algorithm iteration $i = 0$ with the corresponding sensitivity map E_{LL} directly below (panel (e)) and the initial level set function ψ_0 in panel (i). Two intermediate component shapes are shown in panels (b) and (c), and the final optimised shape is shown in panel d. The minimum sensitivity E_{LL}^* varying with iteration i during the optimisation is shown in plot (m). The mean of the velocity term $v_i(\mathbf{x})$ in Equation 14 is shown in plot (n) and the volume residual $V_i(\Omega_i) - V_{req}$ as a function of iteration i is shown in plot (o).

[[Image]]

Figure 8: The example component considered in Figure 7 is reconsidered with a constrained design given by the mask M. a) The mask M used in Equation (17) for the constrained optimisation. The initial shape boundary $\partial\Omega_0$ is shown as a black dotted line. b) The optimised shape with a masking constraint. c) The evolution of the minimum sensitivity E_{LL}^* as the algorithm iterates. d) The evolution of the volume fraction residual ($V_i(\Omega) - V_{req}$) as the algorithm iterates.

3.2 Constraining optimisation with masking

Masking allows for a constraint on the admissible shapes which reduces large deviations from the initial component shape. A constrained optimisation problem for the same square initial shape as in the previous example is now presented. The mask M is prescribed to be a set distance from the boundary $\partial\Omega$ via

$$M(\mathbf{x})\begin{cases}=0 & \text{if } \min|\mathbf{x}-\partial\Omega|>d\\ =1 & \text{if } \min|\mathbf{x}-\partial\Omega|<d\end{cases} \tag{20}$$

where the envelope width $\delta = 2d$, measured in pixels (illustrated in Fig. 1b). A mask M where $\delta = 4$ pixels is shown in Figure 8a and the optimisation is performed with the same discretisation and parameters as above. The final shape is shown in Figure 8b and the evolution of the minimum sensitivity E^*_{LL} during the optimisation is shown in Figure 8c, where E^*_{LL} increases by approximately 20% compared to the initial shape. Understandably, the sensitivity for the unconstrained shape (Fig. 7) is higher than for the constrained case, however there is less resemblance to the initial component shape.

3.3 Beam shape optimisation

Now consider the cross-sections of four beam shapes commonly used in construction and engineering: an I-beam (or girder), T-beam (or Tee bar), C-beam (or Channel) and L-beam (or Angle beam), shown in the top row of Figure 9. Shape optimisation is performed via the level set method with three different masks M of increasing envelope thicknesses ($\delta = 2,4,6$ pixels), where greater thickness allows larger perturbations from the initial component shapes; the domains are 100×100 pixels. The same optimisation parameters are used as those in Section 3.1, and the volume of the initial component is preserved ($V_{req} = V_0$). The final shapes for the four initial components, and for the different mask thicknesses are shown in Figure 9. The improvement in the minimum sensitivity E^* is quantified via Q, which is the percentage improvement in E^* ($Q = 100(E^* - E^*_0)/E^*_0$). The values of Q are labelled in the titles of each subplot.

[[Image]]

Figure 9: Level set method optimisation of four commonly used beam shapes (shown in each column): I-beam, Tee Beam, Channel and Angle Beam, using three different masks M with increasing envelope thicknesses ($\delta = 2,4,6$ pixels). The percentage improvement Q in minimum sensitivity E^* is labelled in the subplot titles.

In all cases, there is an improvement in the minimum ultrasound sensitivity E^*, and generally E^* increases as the envelope width δ increases. In cases where only a small perturbation is admissible ($\delta = 2$), E^* increases by as much as 6.3%. Where large perturbations are allowed ($\delta = 6$), E^* increases by as much as 20.4%. Some similarities are noticeable for the optimal shapes for each of the four component cross-sections. Both concave and convex corners become more rounded, and indentations or protrusions are added to flat surfaces. These perturbations allow for a greater range of incident angles for the ultrasonic transmission and receiver points, therefore improving ultrasonic sensitivity. These more complex designs are more challenging to build using conventional manufacturing techniques, however additive manufacturing can easily manufacture such intricate structures.

In these examples, only the ultrasonic sensitivity is optimised. In practice, the strength and stiffness of the beam would also need to be considered, as any change in shape also alters the beam mechanical properties. Such additional constraints can be factored into future optimisations.

3.4 TFM Imaging

While the use of ultrasonic sensitivity maps (for example E_{LL}) is useful for the calculation of a misfit function and the evolution of the level set function, the ability to image a defect, so that the defect size and position can be better estimated, is fundamental to ultrasonic NDT. To quantify the improvement in the imaging methods following the optimisation of a component's shape, full matrix capture (FMC) data is synthetically generated for a point defect (or point scatterer) located at the point $\mathbf{x}^*$ (the location of the minimum sensitivity E^*_{LL}). That is

$$\mathbf{x}^* = \underset{\mathbf{x}\in\Omega}{\operatorname{argmin}} : E_{LL}(\mathbf{x}). \tag{21}$$

The analytical expressions stated in Equations (3-6) give the recorded amplitude of a point scatterer, and the arrival time of the recorded energy t_{sr} is given by Equation (8). The reflectivity P is calculated as

$$P(t;s,r,\mathbf{x}^*) = \frac{S_L(\theta_s(\mathbf{x}^*))R_L(\theta_r(\mathbf{x}^*))}{[d_s(\mathbf{x}^*)d_r(\mathbf{x}^*)]^{1/2}}\delta(t - t_{sr}(\mathbf{x}^*)) \tag{22}$$

where δ is a unit impulse function. A 3 MHz Ricker wavelet ($\xi(t)$) is used for the source-time function, and a synthetic recorded signal A (or A-scan) for source s, receiver r and scattering point $\mathbf{x}^*$ is then generated by convolving $P(t)$ with the wavelet $\xi(t)$, via

$$A(t;s,r,\mathbf{x}^*) = P(t;s,r,\mathbf{x}^*) * \xi(t) + N(\sigma,t) \quad (23)$$

where $N(\sigma,t)$ is random Gaussian noise with standard deviation σ. A-scans for every source-receiver combination are generated to produce a synthetic full matrix capture dataset.

TFM images were produced using the example initial square component shown in Figure 7a and the optimised disk shape component shown in Figure 7d, (Fig. 10a and 10b, respectively), where the scattering point $\mathbf{x}^*$ is located in the centre of each component. Gaussian noise N with a standard deviation $\sigma = 0.1P_{max}$ is used for both data sets, where P_{max} is the maximum amplitude measured across both shapes $P_{max} = \max_{\Omega} |P|$. An image is then generated using the total focusing method via Equation (7), where the amplitudes in A are normalised to correct for two-dimensional geometric spreading $u(t;s,r,\mathbf{x}^*) = A(t;s,r,\mathbf{x}^*)/(V_P t)^2$. To account for different numbers of source-receiver pairs, which use different amounts of input energy, the intensities I are normalised by the number of source-receiver pairs N^2. Conventionally, TFM images are plotted in decibels, normalised to the maximum amplitude in the respective image ($dB = 20\log_{10}(I_{max}/I)$). The resulting TFM images are shown in Figures 10a and b, and transects of these images shown relative to the true locations of the defects $\mathbf{x}^*$ are show in Figure 10c. To highlight the improvement in the signal-to-noise ratio (SNR), the intensity values in the transect through the initial component shape image I^{init} are normalised with respect to the maximum intensity of the optimised image (I^{opt}_{max}), and plotted as the yellow line in Fig. 10c. The image for the optimised shape has a higher peak amplitude at the defect location and relative to the background material compared to the image for the initial shape; there is an 8 dB improvement in the flaw image when using the optimised design. When estimating the size of a defect, the -6 dB threshold is commonly used in NDT [10]. Using this approach the estimated defect width in the initial and optimised components is 7.4 mm and 3.9 mm, respectively, where the true defect width is 3.0 mm, so the percentage error in sizing the defect is reduced from $100\times(7.3-3)/3 = 147\%$ to $100\times(3.9-3)/3 = 30\%$. The results for the optimised shape are therefore more robust to the addition of background noise and more accurate in estimating the size of a defect.

[[Image]]

Figure 10: Comparison of total focusing method images of a point scatterer for a) the initial and b) the optimised shape (from the optimisation shown in Figure 7). c) Transects through the images

compared with the true defect boundary width (dashed black line).

4 Discussion

4.1 Limitations

This is the first presentation of a framework for shape optimisation that includes NDT considerations. There are several limitations and potential extensions to the presented method. The forward modelling approach uses an analytical model for the transmission and reception of laser induced ultrasound [3, 29, 44]. This model is a first-order scattering approximation (waves are reflected only once by a scatterer), and therefore does not consider any boundary reflections. Ray tracing algorithms that account for reflections (e.g., Bai et al. [2]) or numerical simulation of wave propagation [30, 33] could be implemented to include second order scattering better representing the physics of wave propagation in practice. In addition to this, the optimisation only considers the propagation of compressional (or longitudinal) waves (Equations (3) and (5)). A weighted combination of compressional and transverse wave components [40] could be included in a future implementation.

As the analytical model for the transmission and reception of laser induced ultrasound only considers wave propagation in two dimensions, the shape optimisations presented here only consider the perturbation of the two-dimensional cross-section of a three-dimensional component (rods and beams) to enhance NDT capability. Current compliance-based level set shape and topology optimisation algorithms are capable of designing intricate three-dimensional structures [21]. In principle, our method can be applied similarly to more complex three-dimensional geometries providing the analytical model that generates the ultrasonic wave propagation can account for three dimensions.

Another simplification as presented here is the lack of topological variations during the level set optimisation (i.e., there are no holes in Ω and no new holes are nucleated). Optimising for the topology of a component is a major advantage of the level set method [1, 7], and is particularly important in compliance-minimisation (stiffness maximisation) problems, where a stiff component needs to be designed with a material volume constraint, so the nucleation of void regions is desirable. For ultrasonic NDT applications, the nucleation of voids introduces reflectors and barriers to wave propagation, and therefore could cause difficulties for NDT. The extension of this method to allow topological variations would be a natural extension to the current method; for example allowing for joint optimisation for compliance and ultrasonic sensitivity.

4.2 Experimental Design and Joint Optimisation

In all the examples presented here, there is full coverage of the domain boundary by sources and receivers, that is data is generated and recorded at every point on the boundary of a shape. Realistically, such dense arrays of source and receiver locations are impractical, both due to the time required to collect data as well as the memory requirements for such large datasets. *Experimental design* describes a field of study that seeks to maximise the information in measured data by optimising parameters, such as the number and distribution of sensors, while adhering to some constraint on the cost of the experiment [9, 24]. The sensitivity of ultrasonic NDT (E) depends on the distribution Γ of source s and receivers r, the material properties Ξ, and the spatial domain of the component Ω, and as shown earlier $E(\mathbf{x}, \mathbf{l}, \Xi, \Omega)$. This paper has primarily focused on the optimisation of the spatial domain Ω, however an optimisation of the source and receiver locations Γ or material properties Ξ, or a joint optimisation for Ω, Ξ and Γ could be implemented.

To briefly illustrate this for an arbitrary component, an optimisation on the distribution of sources and receivers Γ is performed for a randomly generated convex polygon with ten vertices (Fig. 11), so that E_{LL}^{*} is maximised via

$$\Gamma^{*} = \underset{\Gamma \in \partial\Omega}{\arg\max}\, E_{LL}(\Gamma, \Xi, \Omega) \tag{24}$$

where Ξ and Ω are held constant. As there are few degrees of freedom, a genetic algorithm can be implemented (see appendix for algorithm information). An additional alternative approach is an iterative grid search algorithm (IGSA, described in Algorithm 1). The IGSA iterates through the desired number of source/receiver elements n_1, performing a grid search for each element to maximise E_{LL}^{*}. This grid search is repeated for all elements a total of n_2 times. Here the number of elements $n_1 = 10$, and the number of iterations $n_2 = 3$ (here the total number of grid search optimisations is $n_1 \times n_2 = 30$).

Algorithm 1: Iterative grid search source and receiver optimisation algorithm. I is the iteration and n_2 is the maximum number of iterations. n_1 is the number of sources/receivers and J is the index of each element (source/receiver location).

---

begin

$I = 1$;

$J = 1$;

while $I \leq n_2$ **do**

while $J \leq n_1$ **do**

$\boldsymbol{\Gamma}_J^* = \underset{\boldsymbol{\Gamma}_J \in \partial\Omega}{\text{argmax}} : E_{LL}^*(\boldsymbol{\Gamma}, \Xi, \Omega)$;

$I = I + 1$;

end

$J = J + 1$;

end

end

[[Image]]

Figure 11: Comparison of the optimal distribution of source/receiver locations $\boldsymbol{\Gamma}^*$ using (a) an iterative grid search method and (b) genetic algorithm. The source/receiver locations are shown as red circles.

The results are shown for the same component spatial domain Ω in Figure 11. The iterative grid search method converges with a higher minimum sensitivity E_{LL}^* and is less computationally expensive. Such optimisations could be included in the current framework for shape optimisation, such that the shape is optimised to maximise E^*, but where the minimum sensitivity E^* is calculated for the optimal distribution of a practical number of sources/receiver locations for each shape considered.

5 Conclusion

A framework for including shape optimisation for ultrasonic non-destructive testing (NDT) in the design of a component has been presented. Ultrasonic sensitivity maps are used to assess the NDT suitability of a component using analytical expressions for the sensitivity of laser induced ultrasound for detecting internal point scatterers. The optimal design of an I-beam cross-section, obtained using a low number of degrees of freedom shape parameterisation and a genetic algorithm, was implemented, and the ultrasonic sensitivity improved by a factor of two while remaining within a design envelope. A level set method was then developed as a high number of degrees of freedom (continuum) approach for shape optimisation for NDT on a range of commonly used beam structures. Up to 20% improvement in ultrasonic sensitivity was achieved in

the case where design envelope and volume constraints were implemented. Flaw images computed using the total focusing method on data arising from the inspection of the optimised shapes were shown to be more robust to the presence of background noise, allowing for more accurate and precise characterisation of internal defects; quantitatively there was an 8 dB improvement in SNR and a five-fold improvement in the estimate of flaw size. Overall, these results show significant potential for the use of a 'Design for Testing' framework to improve NDT capabilities and facilitate efficient maintenance, life extension and remanufacturing processes, in turn minimizing production costs and material waste.

6 Appendix: Genetic algorithm parameters

Table 2: The MATLAB (2019b) function `ga` (global optimization toolbox) parameters used for shape Ω and source/receiver geometry Γ optimisations.

Genetic algorithm parameter	Ω **optimisation (Fig. 4)**	Γ **optimisation (Fig. 11)**
Population size	50	200
Generations	500	1000
Cross-over fraction	0.8	0.8
Elite count fraction	0.05	0.05
Mutation (MATLAB function)	`mutationgaussian: shrink=1,scale=1`	`mutationgaussian: shrink=1,scale=1`

7 Acknowledgments

This work was funded by the Engineering and Physical Sciences Research Council (UK): grant number EP/P005268/1.

8 Data Availability

The raw/processed data required to reproduce these findings cannot be shared at this time as the data also forms part of an ongoing study. Individual MATLAB functions can be made available by request to the authors.

References

[1] G. Allaire, F. Jouve, and A.-M. Toader. Structural optimization using sensitivity analysis and a level-set method. *Journal of computational physics*, 194(1):363–393, 2004.

[2] C. Bai, G. Huang, X. Li, B. Zhou, and S. Greenhalgh. Ray tracing of multiple

transmitted/reflected/converted waves in 2-D/3-D layered anisotropic TTI media and application to crosswell traveltime tomography. *Geophysical Journal International*, 195(2):1068–1087, 2013.

[3] J. R. Bernstein and J. B. Spicer. Line source representation for laser-generated ultrasound in aluminum. *The Journal of the Acoustical Society of America*, 107(3):1352–1357, 2000.

[4] J. P. Blasques and M. Stolpe. Multi-material topology optimization of laminated composite beam cross sections. *Composite Structures*, 94(11):3278–3289, 2012.

[5] A. Blouin, D. Levesque, C. Neron, D. Drolet, and J.-P. Monchalin. Improved resolution and signal-to-noise ratio in laser-ultrasonics by SAFT processing. *Optics Express*, 2(13):531–539, 1998.

[6] P. Cawley. The rapid non-destructive inspection of large composite structures. *Composites*, 25(5):351–357, 1994.

[7] V. J. Challis. A discrete level-set topology optimization code written in Matlab. *Structural and multidisciplinary optimization*, 41(3):453–464, 2010.

[8] J. Chen, J. Xiao, D. Lisevych, and Z. Fan. Laser-induced full-matrix ultrasonic imaging of complex-shaped objects. *IEEE transactions on ultrasonics, ferroelectrics, and frequency control*, 66(9):1514–1520, 2019.

[9] A. Curtis. Optimal design of focused experiments and surveys. *Geophysical Journal International*, 139(1):205–215, 1999.

[10] J. Davies, F. Simonetti, M. Lowe, and P. Cawley. Review of synthetically focused guided wave imaging techniques with application to defect sizing. In *AIP Conference Proceedings*, volume 820, pages 142–149. American Institute of Physics, 2006.

[11] P. Doyle. On epicentral waveforms for laser-generated ultrasound. *Journal of Physics D: Applied Physics*, 19(9):1613, 1986.

[12] M. Dubois, M. Militzer, A. Moreau, and J. F. Bussière. A new technique for the quantitative real-time monitoring of austenite grain growth in steel. *Scripta materialia*, 42(9), 2000.

[13] F. Gibou, R. Fedkiw, and S. Osher. A review of level-set methods and some recent applications. *Journal of Computational Physics*, 353:82–109, 2018.

[14] I. Gibson, D. W. Rosen, B. Stucker, et al. *Additive manufacturing technologies*, volume 17. Springer, 2014.

[15] G. Hatcher, W. Ijomah, and J. Windmill. Design for remanufacture: a literature review and future research needs. *Journal of Cleaner Production*, 19(17-18):2004–2014, 2011.

[16] C. Holmes, B. Drinkwater, and P. Wilcox. The post-processing of ultrasonic array data using the total focusing method. *Insight-Non-Destructive Testing and Condition Monitoring*, 46(11):677–680, 2004.

[17] C. Holmes, B. W. Drinkwater, and P. D. Wilcox. Post-processing of the full matrix of ultrasonic transmit–receive array data for non-destructive evaluation. *NDT & E International*, 38(8):701–711, 2005.

[18] C. Holmes, B. W. Drinkwater, and P. D. Wilcox. Advanced post-processing for scanned ultrasonic arrays: Application to defect detection and classification in non-destructive evaluation. *Ultrasonics*, 48(6-7):636–642, 2008.

[19] W. L. Ijomah, C. A. McMahon, G. P. Hammond, and S. T. Newman. Development of design for remanufacturing guidelines to support sustainable manufacturing. *Robotics and Computer-Integrated Manufacturing*, 23(6):712–719, 2007.

[20] Y. Javadi, C. N. MacLeod, S. G. Pierce, A. Gachagan, D. Lines, C. Mineo, J. Ding, S. Williams, M. Vasilev, E. Mohseni, et al. Ultrasonic phased array inspection of a Wire+ Arc Additive Manufactured (WAAM) sample with intentionally embedded defects. *Additive Manufacturing*, 29:100806, 2019.

[21] S. Kambampati, S. Townsend, and H. A. Kim. Aeroelastic level set topology optimization for a 3D wing. In *2018 AIAA/ASCE/AHS/ASC Structures, Structural Dynamics, and Materials Conference*, page 2151, 2018.

[22] Y. Y. Kim and T. S. Kim. Topology optimization of beam cross sections. *International journal of solids and structures*, 37(3):477–493, 2000.

[23] A. Koneru and K. Chakrabarty. Test and design-for-testability solutions for monolithic 3D integrated circuits. In *Proceedings of the 2019 on Great Lakes Symposium on VLSI*, pages 457–462, 2019.

[24] N. Korta Martiartu, C. Boehm, V. Hapla, H. Maurer, I. J. Balic, and A. Fichtner. Optimal experimental design for joint reflection-transmission ultrasound breast imaging: From ray-to wave-based methods. *The Journal of the Acoustical Society of America*, 146(2):1252–1264, 2019.

[25] J. Liang, W. Xu, C. Yue, K. Yu, H. Song, O. D. Crisalle, and B. Qu. Multimodal

multiobjective optimization with differential evolution. *Swarm and evolutionary computation*, 44:1028–1059, 2019.

[26] D. Lines. Rapid inspection using integrated ultrasonic arrays. *Insight: Non-Destructive Testing and Condition Monitoring*, 40(8):573–577, 1998.

[27] R. T. Lund. Remanufacturing: the experience of the USA and implications for the developing countries. *New York: World Bank Technical Papers, ISSN*, pages 0253–7494, 1984.

[28] J. Luo, Z. Luo, L. Chen, L. Tong, and M. Y. Wang. A semi-implicit level set method for structural shape and topology optimization. *Journal of Computational Physics*, 227(11):5561–5581, 2008.

[29] G. Miller and H. Pursey. The field and radiation impedance of mechanical radiators on the free surface of a semi-infinite isotropic solid. *Proceedings of the Royal Society of London. Series A. Mathematical and Physical Sciences*, 223(1155):521–541, 1954.

[30] P. Moczo, J. O. Robertsson, and L. Eisner. The finite-difference time-domain method for modeling of seismic wave propagation. *Advances in geophysics*, 48:421–516, 2007.

[31] J.-P. Monchalin. Optical detection of ultrasound. *IEEE Transactions on Ultrasonics Ferroelectrics and Frequency Control*, 33:485–499, 1986.

[32] T. Morzadec, D. Marcha, and C. Duriez. Toward shape optimization of soft robots. In *2019 2nd IEEE International Conference on Soft Robotics (RoboSoft)*, pages 521–526. IEEE, 2019.

[33] F. Moser, L. J. Jacobs, and J. Qu. Modeling elastic wave propagation in waveguides with the finite element method. *NDT & E International*, 32(4):225–234, 1999.

[34] M.-H. Noroy, D. Royer, and M. Fink. The laser-generated ultrasonic phased array: Analysis and experiments. *The Journal of the Acoustical Society of America*, 94(4):1934–1943, 1993.

[35] S. Osher, R. Fedkiw, and K. Piechor. Level set methods and dynamic implicit surfaces. *Appl. Mech. Rev.*, 57(3):B15–B15, 2004.

[36] D. Pieris, T. Stratoudaki, Y. Javadi, P. Lukacs, S. Catchpole-Smith, P. D. Wilcox, A. Clare, and M. Clark. Laser induced phased arrays (LIPA) to detect nested features in additively manufactured components. *Materials & Design*, 187:108412, 2020.

[37] J. Plocher and A. Panesar. Review on design and structural optimisation in additive

manufacturing: Towards next-generation lightweight structures. *Materials & Design*, page 108164, 2019.

[38] B. Raj, T. Jayakumar, and M. Thavasimuthu. *Practical non-destructive testing*. Woodhead Publishing, 2002.

[39] A. Riboni, L. Guglielmo, M. Orrù, P. Braione, and G. Denaro. Design for testability of ERMTS applications. In *2019 IEEE International Symposium on Software Reliability Engineering Workshops (ISSREW)*, pages 128–136. IEEE, 2019.

[40] L. Rose. Point-source representation for laser-generated ultrasound. *The Journal of the Acoustical Society of America*, 75(3):723–732, 1984.

[41] L. W. Schmerr. *Fundamentals of ultrasonic nondestructive evaluation*. Springer, 2016.

[42] J. A. Sethian. *Level set methods and fast marching methods: evolving interfaces in computational geometry, fluid mechanics, computer vision, and materials science*, volume 3. Cambridge university press, 1999.

[43] W. Song and A. Keane. A study of shape parameterisation methods for airfoil optimisation. In *10th AIAA/ISSMO Multidisciplinary analysis and optimization conference*, page 4482, 2004.

[44] T. Stratoudaki, M. Clark, and P. D. Wilcox. Laser induced ultrasonic phased array using full matrix capture data acquisition and total focusing method. *Optics express*, 24(19):21921–21938, 2016.

[45] T. Stratoudaki, Y. Javadi, W. Kerr, P. D. Wilcox, D. Pieris, and M. Clark. Laser induced phased arrays for remote ultrasonic imaging of additive manufactured components. In *57th Annual Conference of the British Institute of Non-Destructive Testing, NDT 2018*, pages 174–182, 2018.

[46] K. M. Tant, E. Galetti, A. Mulholland, A. Curtis, and A. Gachagan. A transdimensional bayesian approach to ultrasonic travel-time tomography for non-destructive testing. *Inverse Problems*, 34(9):095002, 2018.

[47] K. M. Tant, A. J. Mulholland, A. Curtis, and W. L. Ijomah. Design-for-testing for improved remanufacturability. *Journal of Remanufacturing*, 9(1):61–72, 2019.

[48] K. M. M. Tant, E. Galetti, A. Mulholland, A. Curtis, and A. Gachagan. Effective grain orientation mapping of complex and locally anisotropic media for improved imaging in ultrasonic non-destructive testing. *Inverse Problems in Science and Engineering*, pages

1–25, 2020.

[49] L.-S. Wang, J. S. Steckenrider, and J. D. Achenbach. A fiber-based laser ultrasonic system for remote inspection of limited access components. In *Review of Progress in Quantitative Nondestructive Evaluation*, pages 507–514. Springer, 1997.

[50] M. Y. Wang, X. Wang, and D. Guo. A level set method for structural topology optimization. *Computer methods in applied mechanics and engineering*, 192(1-2):227–246, 2003.

[51] R. M. White. Generation of elastic waves by transient surface heating. *Journal of Applied Physics*, 34(12):3559–3567, 1963.

[52] D. Whitley. A genetic algorithm tutorial. *Statistics and computing*, 4(2):65–85, 1994.

[53] P. D. Wilcox. Ultrasonic arrays in NDE: Beyond the B-scan. In *AIP Conference Proceedings*, volume 1511, pages 33–50. American Institute of Physics, 2013.

[54] K. R. Yawn, M. A. Osterkamp, D. Kaiser, and C. Barina. Improved laser ultrasonic systems for industry. In *AIP Conference Proceedings*, volume 1581, pages 397–404. American Institute of Physics, 2014.

Declaration of interests

☒ The authors declare that they have no known competing financial interests or personal relationships that could have appeared to influence the work reported in this paper.

☐The authors declare the following financial interests/personal relationships which may be considered as potential competing interests:

- A design-for-testing framework for ultrasonic non-destructive testing suitability
- A novel implementation of the level set method based on ultrasonic coverage maps
- Optimised shapes lead to improved flaw detection
- Optimised shapes lead to more accurate estimates of defect size

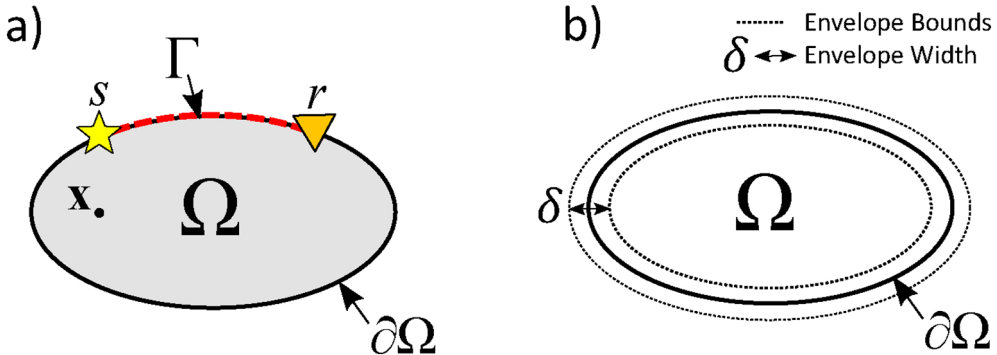

Figure 1

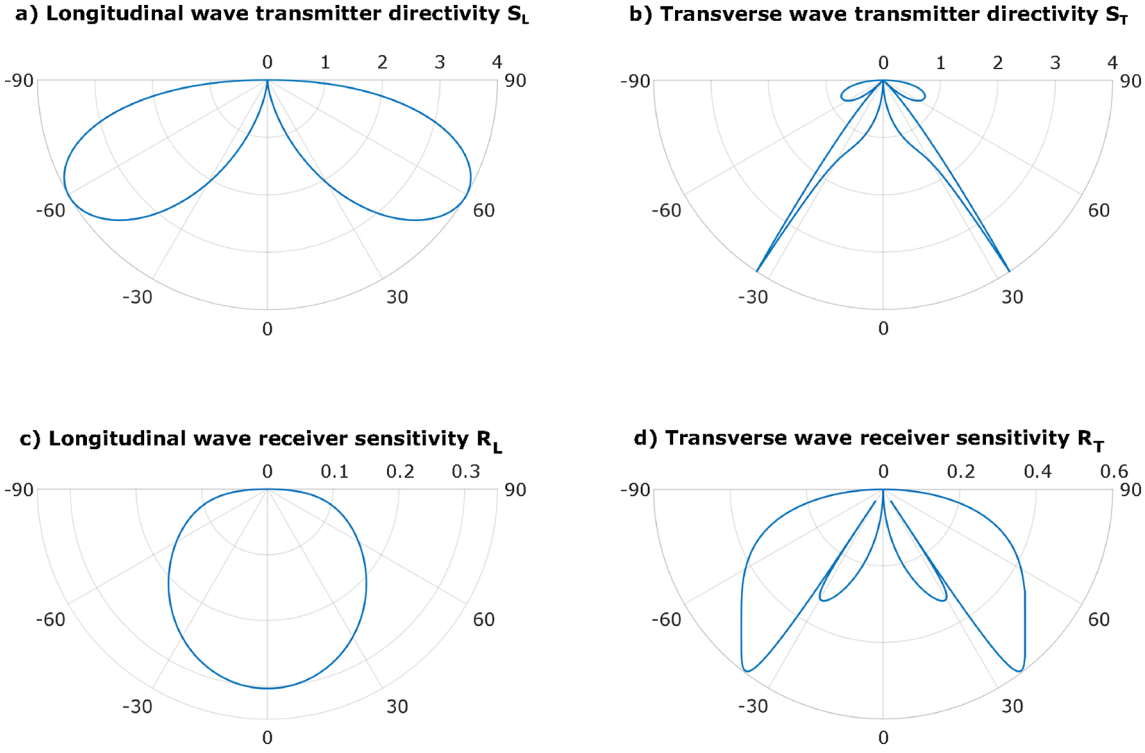
a) Longitudinal wave transmitter directivity S_L
0
1
2
3
4
-90
90
-60
60
-30
30
0
b) Transverse wave transmitter directivity S_T
0
1
2
3
4
-90
90
-60
60
-30
30
0
c) Longitudinal wave receiver sensitivity R_L
0
0.1
0.2
0.3
-90
90
-60
60
-30
30
0
d) Transverse wave receiver sensitivity R_T
0
0.2
0.4
0.6
-90
90
-60
60
-30
30
0

Figure 2

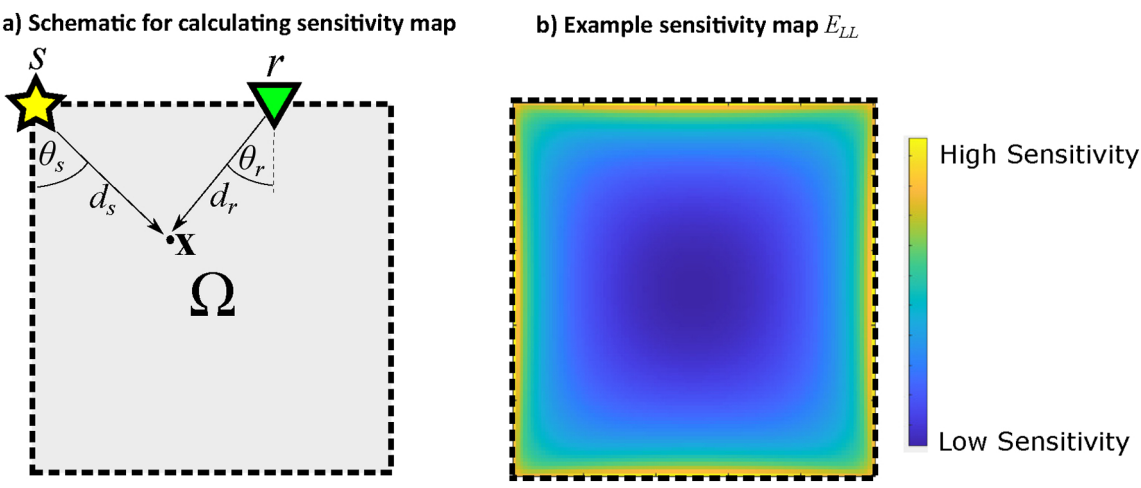
a) Schematic for calculating sensitivity map
b) Example sensitivity map E_{LL}
s
r
θ_s
θ_r
d_s
d_r
$\mathbf{x}$
Ω
High Sensitivity
Low Sensitivity

Figure 3

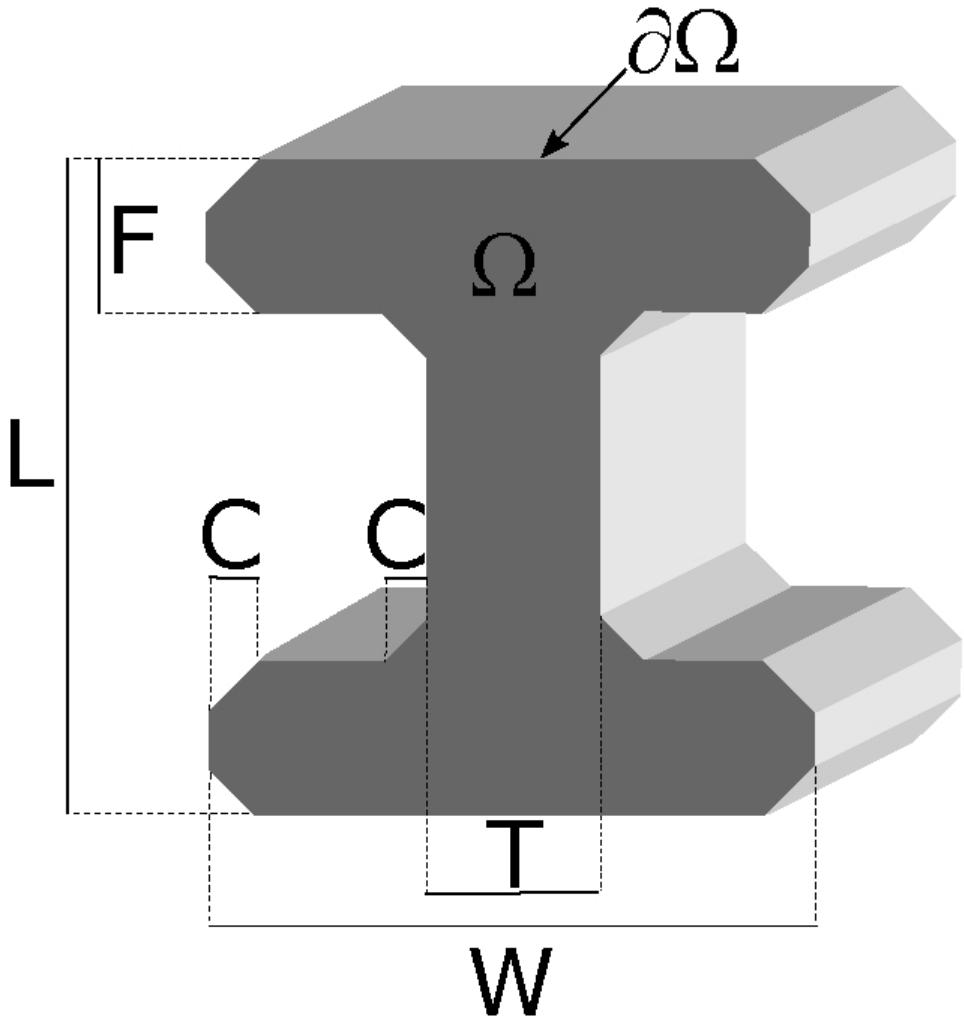

L = Length
W = Width
F = Flange thickness
T = Web thickness
C = Corner depth

Figure 4

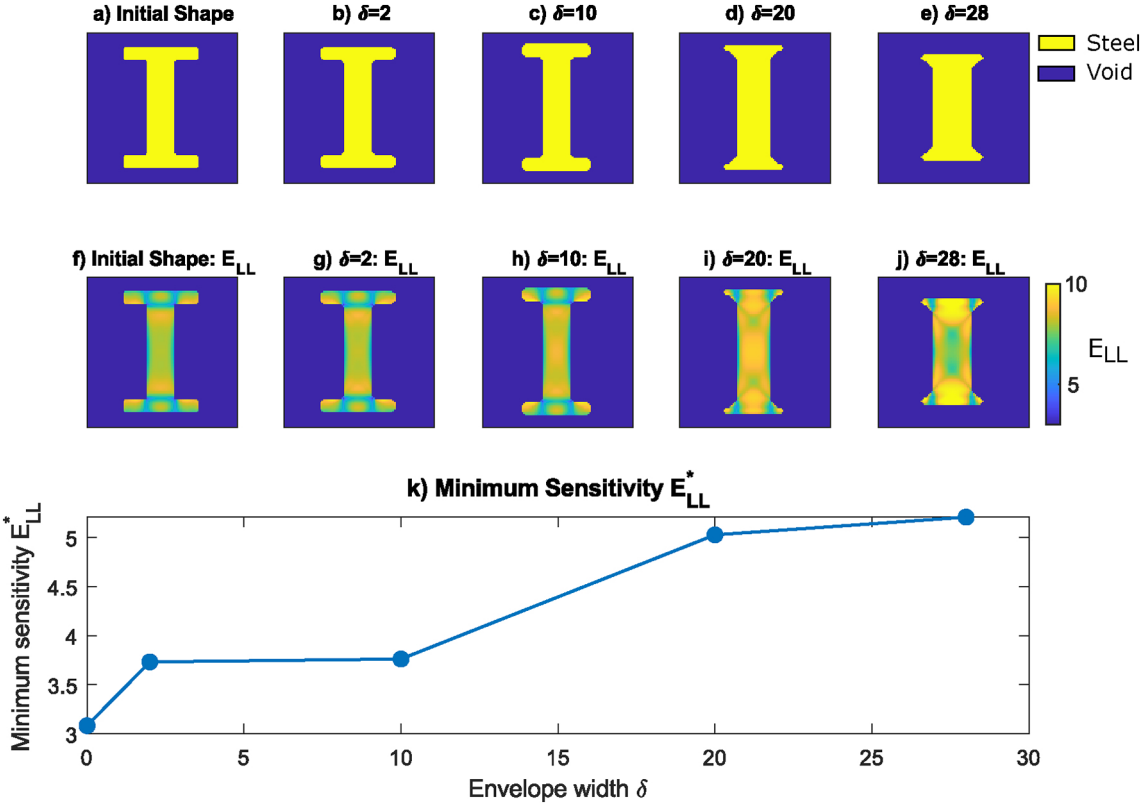
a) Initial Shape
b) δ=2
c) δ=10
d) δ=20
e) δ=28
Steel
Void
f) Initial Shape: E_LL
g) δ=2: E_LL
h) δ=10: E_LL
i) δ=20: E_LL
j) δ=28: E_LL
10
E_LL
5
k) Minimum Sensitivity E*_LL
Minimum sensitivity E*_LL
5
4.5
4
3.5
3
0
5
10
15
20
25
30
Envelope width δ

Figure 5

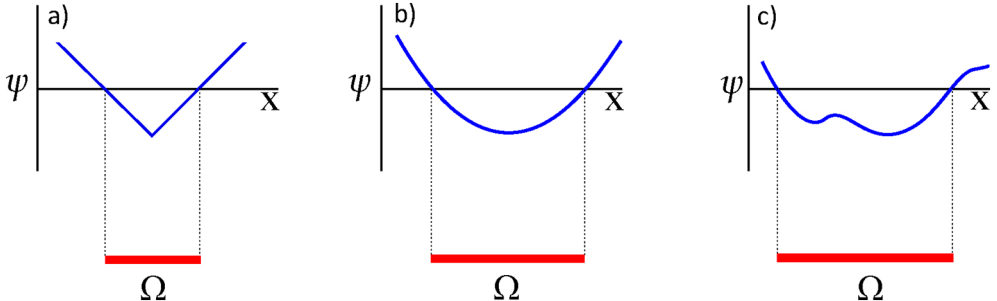

Figure 6

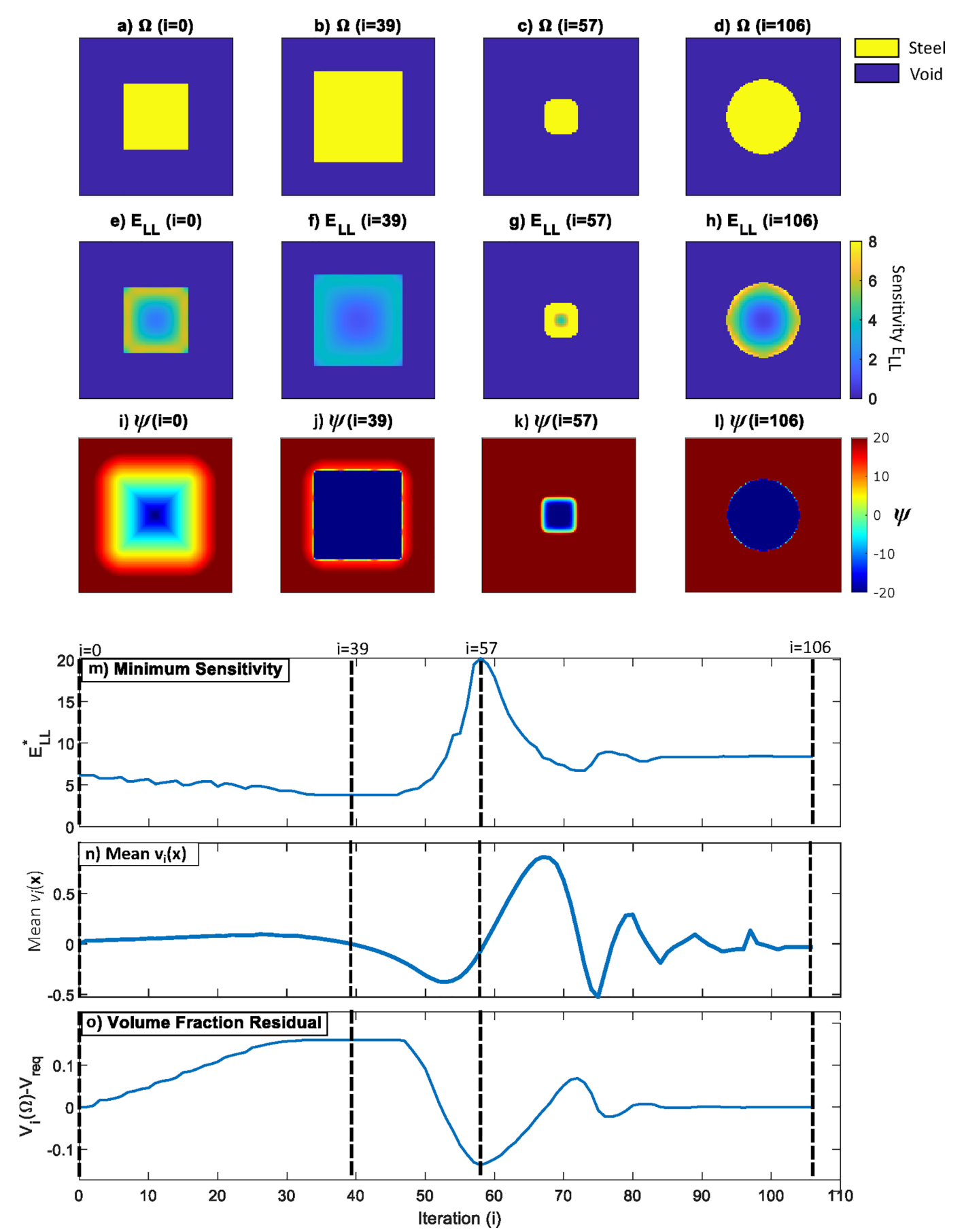
a) Ω (i=0)
b) Ω (i=39)
c) Ω (i=57)
d) Ω (i=106)
Steel
Void
e) E_LL (i=0)
f) E_LL (i=39)
g) E_LL (i=57)
h) E_LL (i=106)
Sensitivity E_LL
i) ψ (i=0)
j) ψ (i=39)
k) ψ (i=57)
l) ψ (i=106)
ψ
i=0
i=39
i=57
i=106
m) Minimum Sensitivity
E*_LL
n) Mean v_i(x)
Mean v_i(x)
o) Volume Fraction Residual
V_i(Ω)-V_req
Iteration (i)

Figure 7

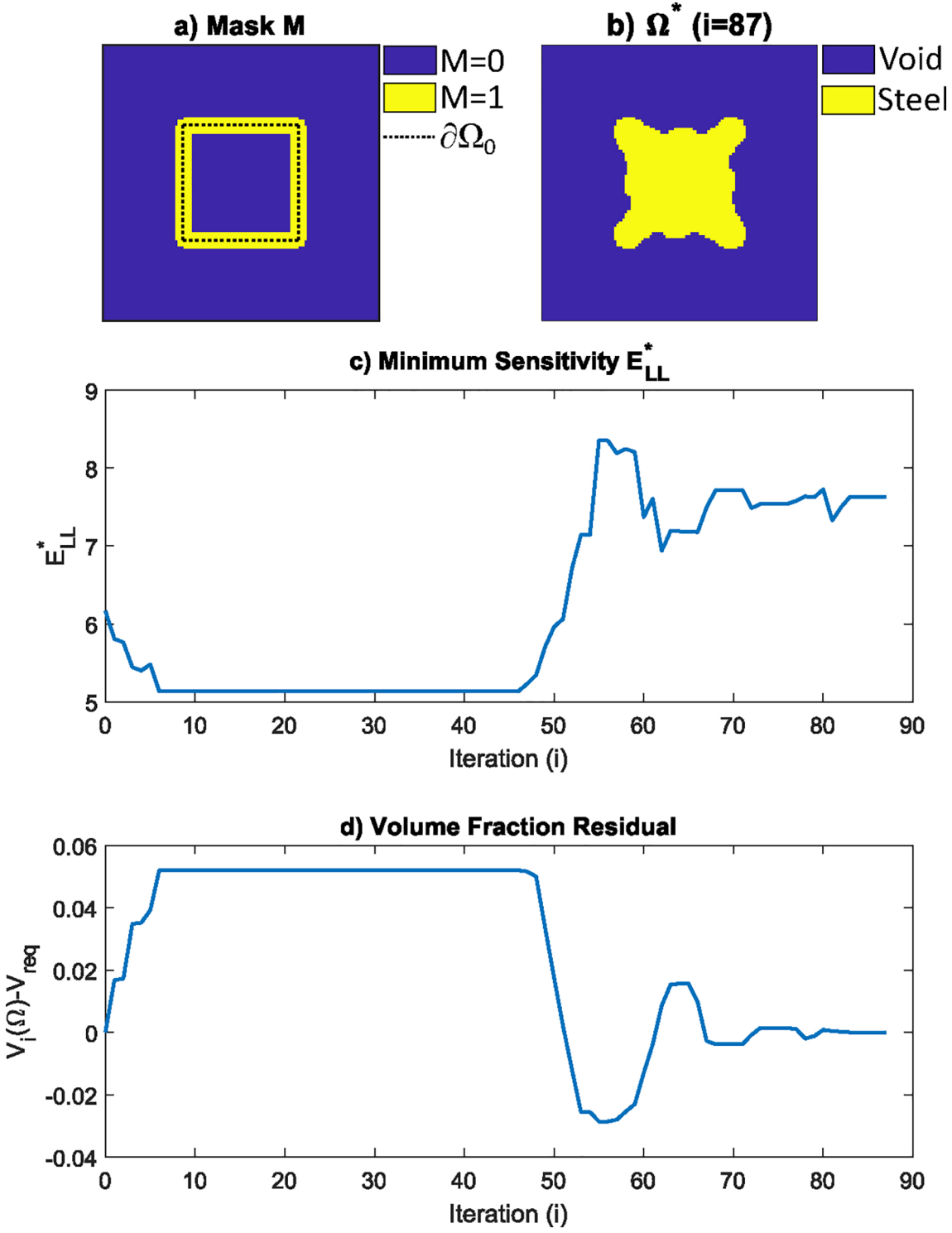
a) Mask M
M=0
M=1
$\partial\Omega_0$
b) Ω^* (i=87)
Void
Steel
c) Minimum Sensitivity E^*_{LL}
E^*_{LL}
Iteration (i)
d) Volume Fraction Residual
$V_i(\Omega)-V_{req}$
Iteration (i)

Figure 8

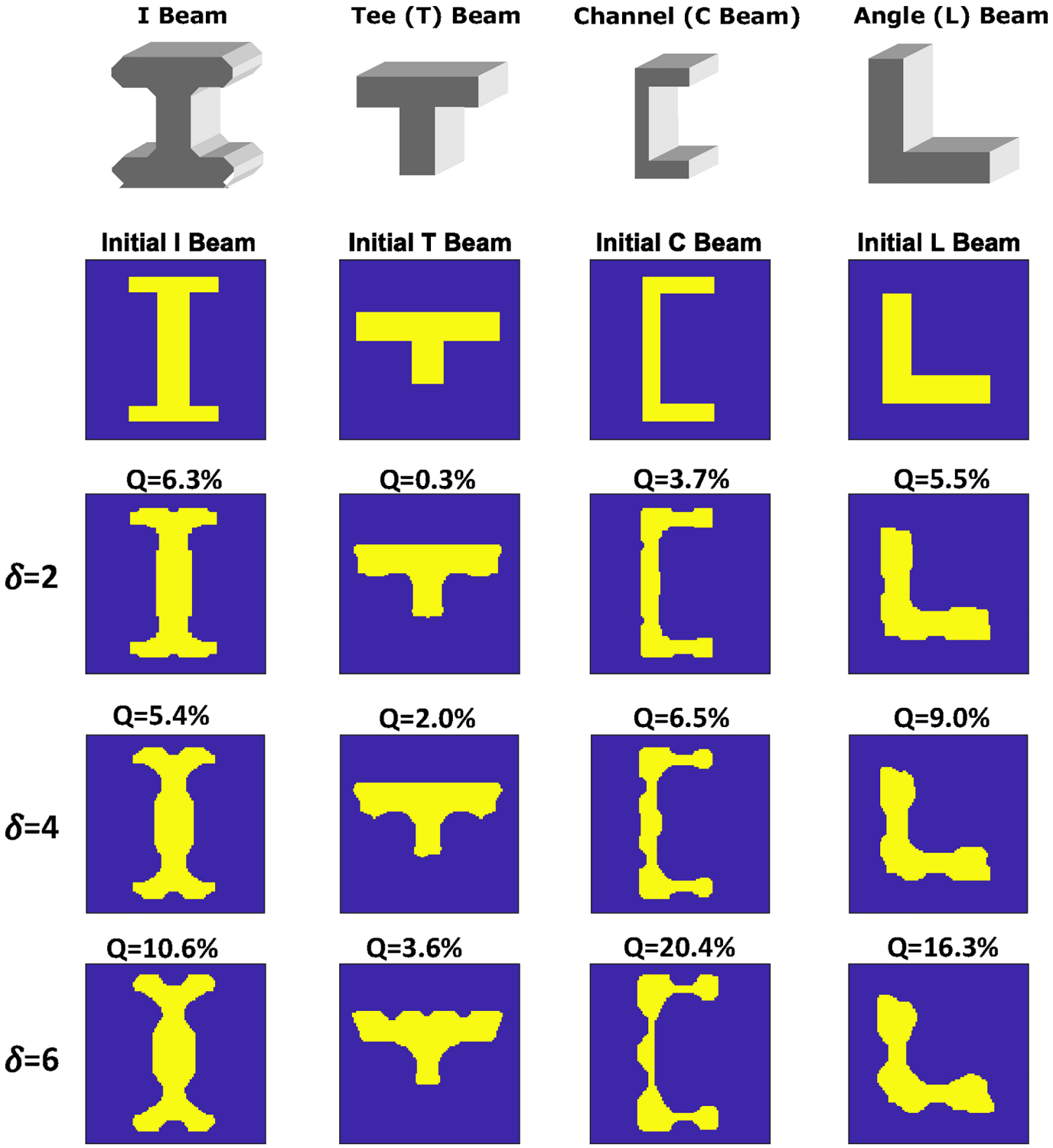
I Beam
Tee (T) Beam
Channel (C Beam)
Angle (L) Beam
Initial I Beam
Initial T Beam
Initial C Beam
Initial L Beam
Q=6.3%
Q=0.3%
Q=3.7%
Q=5.5%
δ=2
Q=5.4%
Q=2.0%
Q=6.5%
Q=9.0%
δ=4
Q=10.6%
Q=3.6%
Q=20.4%
Q=16.3%
δ=6

Figure 9

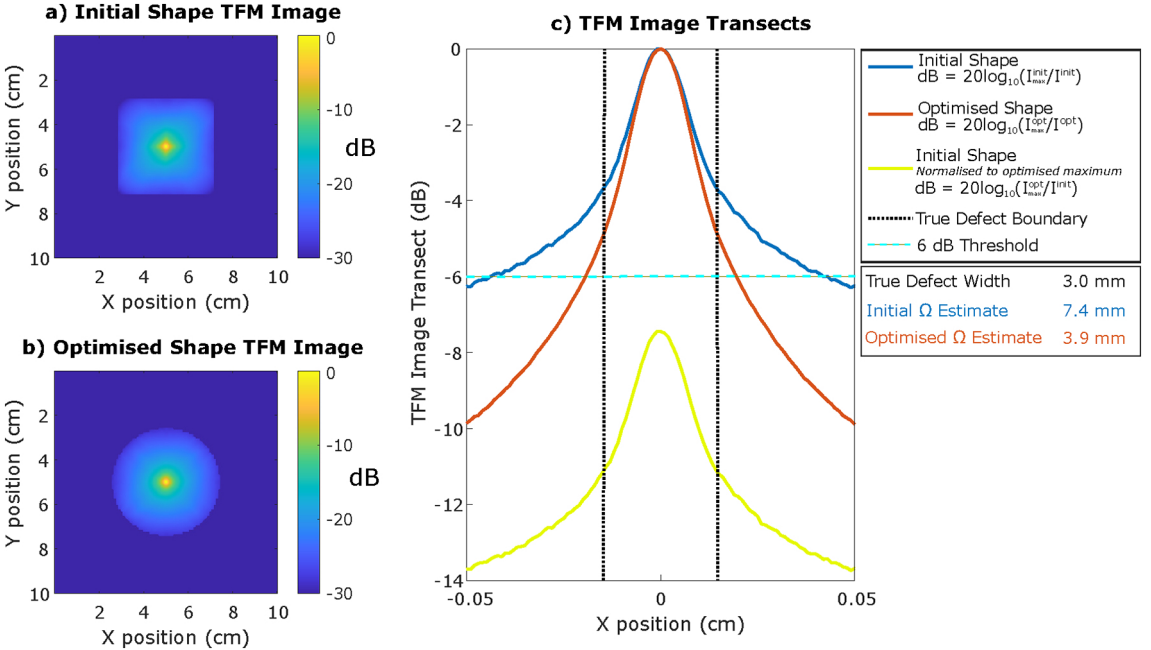
a) Initial Shape TFM Image
Y position (cm)
X position (cm)
dB
b) Optimised Shape TFM Image
Y position (cm)
X position (cm)
dB
c) TFM Image Transects
TFM Image Transect (dB)
X position (cm)
Initial Shape
dB = 20log10(I^init_max/I^init)
Optimised Shape
dB = 20log10(I^opt_max/I^opt)
Initial Shape
Normalised to optimised maximum
dB = 20log10(I^opt_max/I^init)
True Defect Boundary
6 dB Threshold
True Defect Width 3.0 mm
Initial Ω Estimate 7.4 mm
Optimised Ω Estimate 3.9 mm

Figure 10

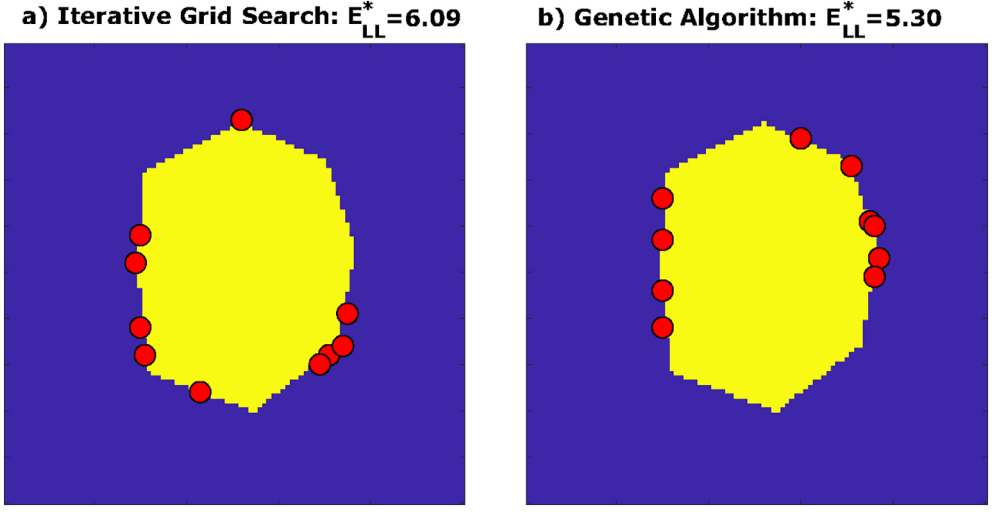

Figure 11